

# Effect of Cerium on the Nucleation and Microstructure of High-Strength Low-Alloy Steel During Solidification



Fei Huang and Jing Li

**Abstract** The effect of cerium on the solidification nucleation and microstructure of high-strength low-alloy steel was investigated. The in situ observation, inclusion characterization and microstructure analysis were performed via high temperature confocal laser scanning microscopy, scanning electron microscope, and electron backscatter diffraction. The results showed that Ce significantly increased the nucleation site density. After cerium treatment, the solidification temperature range and time were decreased by 17.6 °C and 22.44 s, respectively. Based on the Johnson-Mehl-Avrami-Kologoromov theory, the solidification rate constant increased from  $7.59 \times 10^{-5}$  to  $5.68 \times 10^{-4}$  after adding Ce, promoting the phase transformation. The typical inclusions were modified from CaS and CaS+MgAl<sub>2</sub>O<sub>4</sub> to CeAlO<sub>3</sub>+CaS and Ce<sub>2</sub>O<sub>2</sub>S+CaS with an increase in number and a decrease in size when adding Ce. Numerous fine rare earth inclusions could effectively induce the formation of  $\delta$ -Fe and  $\gamma$ -Fe through heterogeneous nucleation, thereby decreasing the average grain size from 13.76 to 12.38  $\mu\text{m}$ .

**Keywords** Cerium treatment · Solidification · Microstructure · In situ observation · Phase transformation

## Introduction

High-strength low-alloy (HSLA) steel has been used in many fields such as storage tanks, construction, bridges, ships and pressure vessels due to the high strength and excellent impact toughness [1, 2]. With the increasing demand for material strength and thickness, higher requirements are put forward for the comprehensive properties of HSLA steel. Refinement of the microstructure is an effective way to improve the properties of steel [3, 4].

---

F. Huang · J. Li (✉)

State Key Laboratory of Advanced Metallurgy, University of Science and Technology Beijing, Haidian District, 30 Xueyuan Road, Beijing 100083, China  
e-mail: [lijing@ustb.edu.cn](mailto:lijing@ustb.edu.cn)

Inclusions are crucial in refining the solidification microstructure. The inclusions could act as the core of heterogeneous nucleation and promote the phase transformation during solidification, thereby refining the grains [5, 6]. Additionally, inclusions could pin the austenite grain boundaries and inhibit the growth of grains [7, 8].

Rare earth can purify the molten steel and micro-alloying, which is of benefit to the inclusions and solidification microstructure. Guan et al. [9] investigated that by adding appropriate RE to the Cr-Ni-Mo hot work die steel, the morphology and distribution of inclusions were improved and fine plate martensite was obtained. Zhao et al. [10] reported that the RE elements could refine the grains and inclusions and change the chemical compositions of the inclusions in the GCr15 bearing steel. Qiao et al. [11] pointed out that the addition of rare earth Ce refined the as-cast microstructure and changed the type of inclusions in the steel. Zhang et al. [12] also indicated that a large number of small-sized rare earth inclusions were distributed at the dendrite cores, promoting the nucleation of  $\gamma$ -Fe during solidification and refining the dendritic structures.

However, extensive research on the rare earths cannot be applied to the practical production due to their active chemical properties. In addition, direct observation of dynamic solidification phenomena through the high temperature confocal laser scanning microscopy (HTCLSM) to determine the influence of rare earth on the solidification process has rarely been studied. Thus, the aim of the present work was to investigate the effect of cerium addition on the solidification nucleation and microstructure in the high-strength low-alloy steel. The specific solidification process of the steel was analyzed by means of HTCLSM and Johnson-Mehl-Avrami-Kolmogorov (JMAK) theory. Moreover, the influence mechanism of Ce on the solidification nucleation and microstructure was revealed by the inclusion characterization, disregistry theory, and electron backscatter diffraction (EBSD) analysis.

## Materials and Experimental Methods

### *Sample Preparation*

The production of experimental steels was mainly divided into four stages, which were basic oxygen furnace  $\rightarrow$  ladle furnace (LF) refining  $\rightarrow$  Ruhrstahl-Heraeus (RH) refining  $\rightarrow$  continuous casting. Deoxidation and desulfurization of the molten steel were completed before the RH refining. During the RH refining, Ce-Fe alloy with the cerium mass fraction of 10% was added to the molten steel. After the vacuum cycling, the Ca-Si wire was added. Lastly, the molten steel was cast into plates via continuous casting. To investigate the effect of cerium on the solidification of steel, steel samples without and with the addition of Ce-Fe alloy were taken and marked S1 and S2, respectively. Comprehensive chemical compositions of the two steel samples are listed in Table 1. The addition of Ce-Fe alloy resulted in the Ce content of 0.002% in the S2 steel.

**Table 1** Chemical compositions of the steel samples (mass %)

Sample	C	Si	Mn	P	Al	Nb	V	Ti
S1	0.1	0.3	1.6	0.01	0.02	0.05	0.07	0.02
S2	0.1	0.3	1.6	0.01	0.03	0.05	0.07	0.02
Sample	Cr	Mo	Ca	S	O	N	Ce	Fe
S1	0.284	0.13	0.002	0.002	0.001	0.003	0	Bal
S2	0.27	0.122	0.001	0.002	0.001	0.003	0.002	Bal

### *In Situ Observation*

Samples were taken from the plates and machined into the cylinder with the diameter of 5 mm and the height of 3 mm. The in situ observation of the solidification was conducted using high temperature confocal laser scanning microscopy. The reaction chamber was vacuumed to 100 MPa and filled with high purity Ar. After grinding and polishing, the samples were placed in the alumina crucibles. The samples were heated at the rate of 200 °C min<sup>-1</sup> to 1550 °C and held for 5 min. Then, they were cooled to the room temperature at the rate of 50 °C min<sup>-1</sup>. To ensure accuracy, each experiment was repeated three times.

### *Inclusion Characterization and EBSD Analysis*

To determine the inclusions in the steel, specimens with the dimensions of 10 mm × 10 mm × 10 mm were cut from the plates. The morphologies, types and compositions of the inclusions in the samples were characterized using scanning electron microscope (SEM, FEI Quanta-250, FEI Corporation, Hillsboro, OR, U.S.A.) and energy-dispersive spectrometer (EDS, XFlash 5030, Bruker, Germany). The INCA Steel automatic detection system of non-metallic inclusion (EVO 18, ZEISS, Germany) was employed to measure the size distribution of inclusions. The scanning area for each sample was 5 × 5 mm<sup>2</sup>, and any inclusion larger than 1 μm in size was included.

For electron backscatter diffraction analysis, the specimens were prepared at the room temperature using electrolytic polishing in an alcohol solution containing 5% perchloric acid. The EBSD was measured using HKL Channel 5 system at 20 keV with samples tilted at 70° and connected to the FEI Scios DualBeam SEM.

## Results and Discussion

### *In Situ Observation of Solidification*

Figures 1 and 2 illustrate the solidification processes of the experimental steels obtained by HTCLSM. It can be seen that the solidification process of steel generally included three stages. In the initial stage of solidification,  $\delta$ -Fe phase was first observed to nucleate in the liquid (L) phase. With the decrease of temperature, the precipitated  $\delta$ -Fe phases gradually grew up and the number of nucleation increased. Then the peritectic reaction ( $L + \delta \rightarrow \gamma$ ) occurred, and the thin layer-like  $\gamma$ -Fe phases nucleated at the junction of the liquid and  $\delta$ -Fe phases, increasingly consuming them to grow. With a further decrease in temperature, the  $\delta$ -Fe phases were no longer observed and the residual liquid phases were completely transformed into  $\gamma$ -Fe phases at the end of solidification. The in situ observation results of the solidification process were consistent with the research of Griesser et al. [13–15]. From the above, the solidification path of the experimental steel was  $L \rightarrow L + \delta \rightarrow L + \delta + \gamma \rightarrow L + \gamma \rightarrow \gamma$ .

The solidification process of the S1 steel observed by HTCLSM is shown in Fig. 1. As shown in Fig. 1, the initial nucleation temperature was 1514.4 °C. After 8 s, the nucleation site density was  $68.58 \text{ mm}^{-2}$ . 16 s later, the nucleation site density was

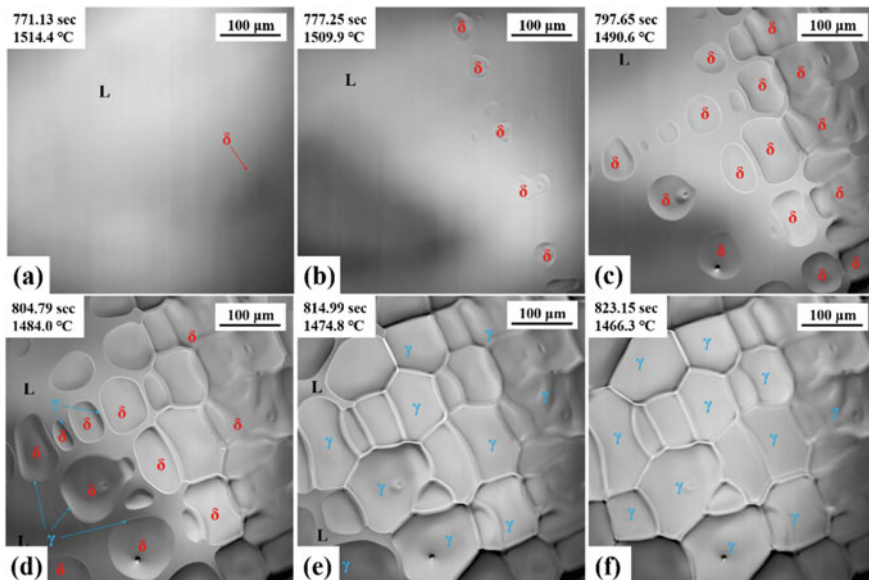


**Fig. 1** Solidification process of the S1 steel observed in situ via HTCLSM

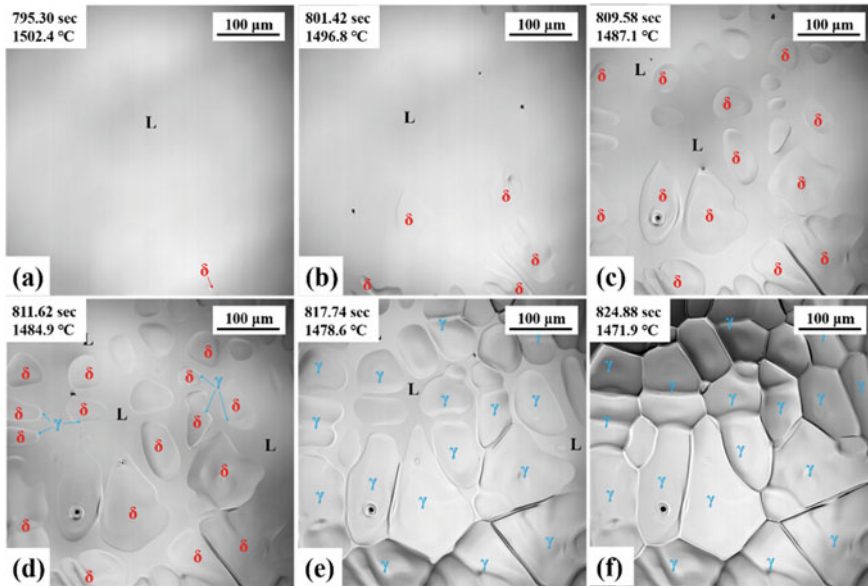


**Fig. 2** Solidification process of the S2 steel observed in situ via HTCLSM

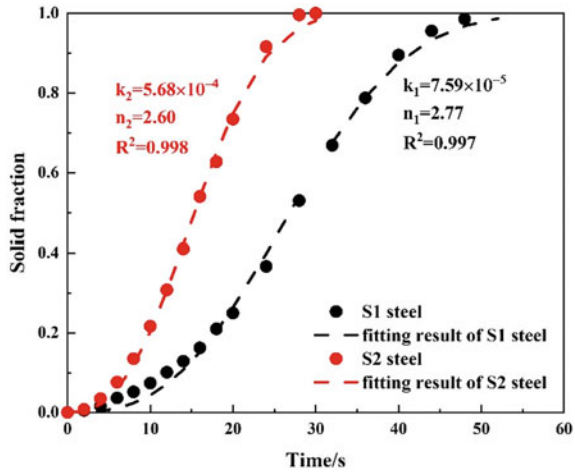
increased to  $107.16 \text{ mm}^{-2}$ . When the temperature decreased to  $1466.3 \text{ }^\circ\text{C}$ , the solidification process was completed. The temperature range and time of solidification were  $48.1 \text{ }^\circ\text{C}$  and  $52.02 \text{ s}$ , respectively.

Figure 2 shows the in situ observation results during solidification of the S2 steel. As shown in Fig. 2, the initial nucleation site appeared at  $1502.4 \text{ }^\circ\text{C}$ . The addition of cerium resulted in the lower initial nucleation temperature of the  $\delta$ -Fe phase. At the initial stage of solidification, rare earth elements were enriched at the solid/liquid interface, hindering the diffusion of atoms. Consequently, the energy barrier for the alloy atoms to reach the  $\delta$ -Fe phase was increased and the initial nucleation temperature of the  $\delta$ -Fe phase was decreased [16]. After 8 and 16 s, the nucleation site density reached  $115.74$  and  $222.90 \text{ mm}^{-2}$ , respectively. In comparison to the Ce-free steel, the nucleation site density of Ce-containing steel was increased by 47.16 and  $115.74 \text{ mm}^{-2}$ , respectively. Rare earth could significantly promote the nucleation of solidification. The solidus temperature was  $1471.9 \text{ }^\circ\text{C}$  in the S2 steel. The temperature range and time of solidification were  $30.5 \text{ }^\circ\text{C}$  and  $29.58 \text{ s}$ , respectively. It was clear that Ce shortened the solidification temperature range and time.

### ***Analysis of the Solidification Process Using the JMAK Theory***

To clarify the influence mechanism of rare earth on the solidification process, the solid fraction at different times was calculated by Image-Pro Plus 6.0 software. The

**Fig. 3** Fitting results of the solid fraction of the experimental steels



solidification transformation was described with the JMAK theory [17]. The JMAK theory is typically shown in Eq. (1).

$$Y = 1 - \exp(-kt^n) \tag{1}$$

where  $Y$  is the solid fraction;  $k$  is the rate constant of solidification, which could characterize the velocity of the solid–liquid phase transformation;  $t$  is time;  $n$  is the Avrami exponent,  $n < 3$  indicates site saturation as the nucleation mechanism, while  $4 > n > 3$  indicates site saturation plus Avrami nucleation as the nucleation mechanism.

The solid fraction and time relationship curves of the experimental steels were analyzed with the equation above, and the fitting results are shown in Fig. 3. According to Fig. 3, the rate constant  $k$  and Avrami exponent  $n$  of the S1 steel were  $7.59 \times 10^{-5}$  and 2.77, respectively. S1 steel was the site saturation nucleation owing to the Avrami exponent being less than 3. After the addition of 0.002% Ce, the Avrami exponent  $n$  of the S2 steel was 2.6, which was still less than 3. The nucleation mechanism did not change. Nevertheless, the rate constant  $k$  was increased to  $5.68 \times 10^{-4}$ . After cerium treatment, the velocity of transformation from liquid to solid phase during the solidification was increased, resulting in a dramatic reduction in the solidification time.

### ***Effect of Cerium on Solidification Nucleation and Microstructure***

Due to the fact that inclusion could act as the core of heterogeneous nucleation, it is an essential factor affecting the solidification nucleation. The EDS spectrums

and element mappings of typical inclusions in the experimental steels are shown in Fig. 4. It can be seen that the typical inclusions in the S1 steel were mainly CaS and CaS+MgAl<sub>2</sub>O<sub>4</sub>. CaS inclusions were spherical or long strip, as shown in Fig. 4a, b. As shown in Fig. 4c, d, the shape of the CaS+MgAl<sub>2</sub>O<sub>4</sub> complex inclusions was irregular. After the addition of rare earth, the typical inclusions in the S2 steel were modified to CeAlO<sub>3</sub>+CaS and Ce<sub>2</sub>O<sub>2</sub>S+CaS complex inclusions, as shown in Fig. 4e–h. From SEM-EDS determination, the area brighter than the steel matrix of the complex inclusions was Ce-containing inclusions, and that darker than the matrix was CaS. The complex inclusions were spherical or ellipsoidal in shape and 1–2 μm in size.

To identify the effect of Ce on the size and number of inclusions, the average size and number density of inclusions in the experimental steels were counted and the results are shown in Fig. 5. As can be seen from Fig. 5, the average size of the inclusions decreased from 2.83 to 1.56 μm, and the number density increased from 46.21 to 64.85 mm<sup>-2</sup> after adding Ce. The results demonstrated that Ce could significantly refine the inclusions in the steel [18, 19] and increase the number of these inclusions.

During solidification, the liquid phase transformed into the δ-Fe and γ-Fe phases. Thus, the effect of CaS, MgAl<sub>2</sub>O<sub>4</sub>, CeAlO<sub>3</sub>, and Ce<sub>2</sub>O<sub>2</sub>S on the promotion of δ-Fe and γ-Fe formation by heterogeneous nucleation was investigated. The possibility of the inclusions acting as the heterogeneous cores could be determined in terms of

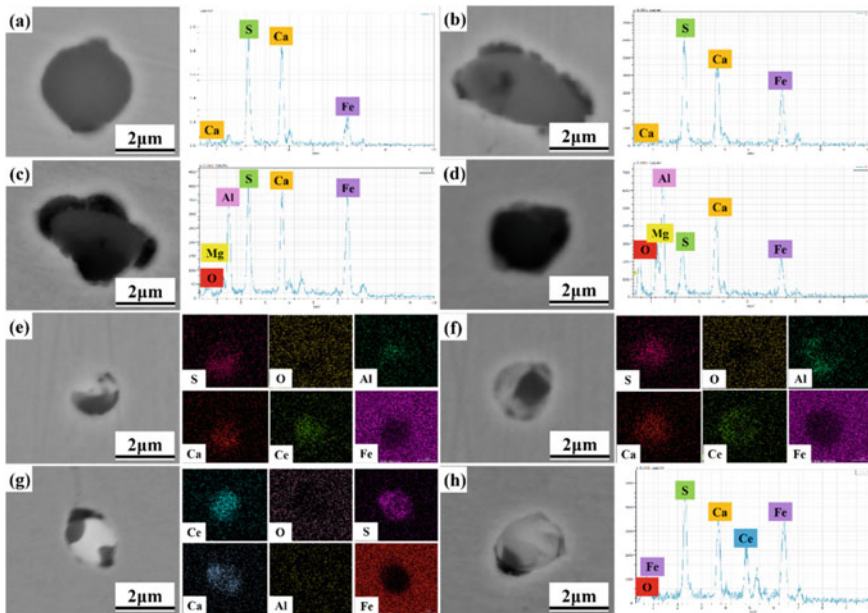
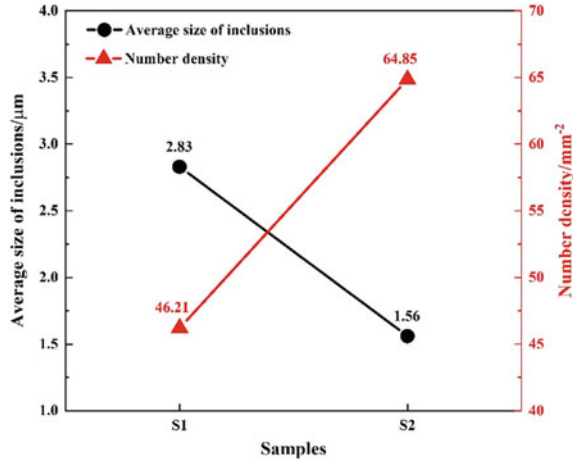


**Fig. 4** SEM images and EDS results of the typical inclusions observed in the experimental steels: a–d S1 steel; e–h S2 steel

**Fig. 5** Number density and average size of inclusions in the experimental steels



the disregistry between the inclusions and the nucleated phases. The disregistry was calculated based on the Bramfitt disregistry theory model, as shown in the following equation [20].

$$\delta_{(hkl)_s}^{(hkl)_n} = \sum_{i=1}^3 \frac{|d[uvw]_s^i \cos \theta - d[uvw]_n^i|}{3} \times 100 \quad (2)$$

where  $i$  is the three lowest-index directions within  $90^\circ$  of the nucleated solid and substrate planes;  $(hkl)_{sn}$  is the low-index plane of the substrate/nucleated solid;  $[uvw]_{sn}$  is the low-index direction of  $(hkl)_s/(hkl)_n$ ;  $d[uvw]_{sn}$  is the interatomic spacing along  $[uvw]_s/[uvw]_n$ ;  $\theta$  is the angle between the  $[uvw]_s$  and  $[uvw]_n$ .

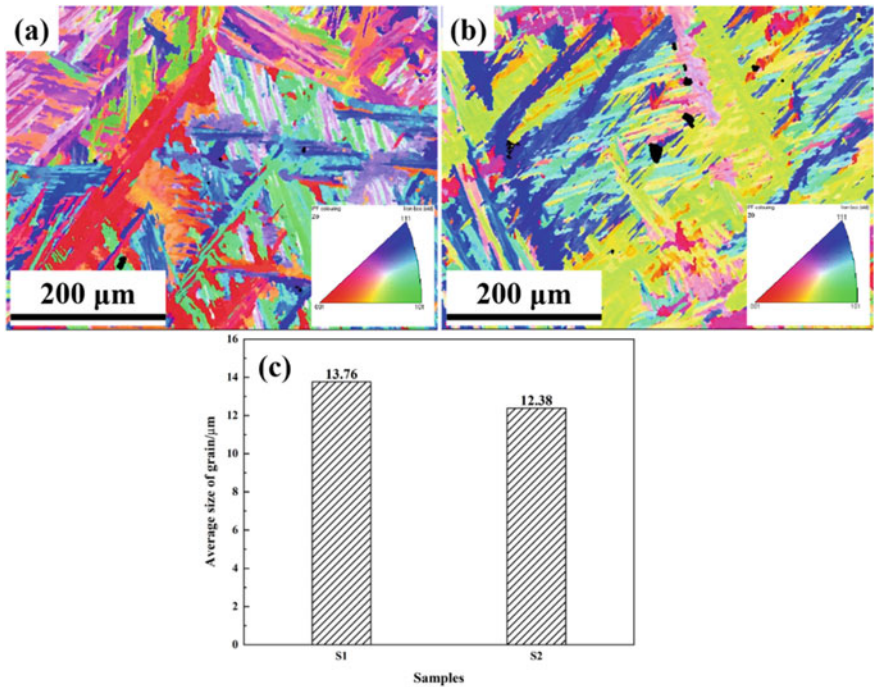
Table 2 presents the relevant parameters and results of the disregistry calculation between inclusions and  $\delta$ -Fe/ $\gamma$ -Fe on the basis of Eq. (2). In accordance with Bramfitt disregistry theory, the substrate could effectively promote the nucleation of the nucleated solid with the disregistry of less than 12%. As can be seen in Table 2, the disregistry results between  $\text{CeAlO}_3/\text{Ce}_2\text{O}_2\text{S}$  inclusions and  $\delta$ -Fe/ $\gamma$ -Fe phases were all less than 12% compared to  $\text{CaS}$  and  $\text{MgAl}_2\text{O}_4$  inclusions. Therefore, the generated rare earth inclusions after Ce treatment were effective in promoting the heterogeneous nucleation of  $\delta$ -Fe and  $\gamma$ -Fe during solidification [21, 22]. Furthermore, the addition of Ce increased the number of inclusions and decreased their size. Ultimately, the number of effective nucleation cores in the liquid steel increased, causing the nucleation site density to increase considerably.

Figure 6 shows the inverse pole figure (IPF) maps and average grain size of the S1 and S2 steel analyzed via EBSD. Compared to the Ce-free steel, the grain distribution of the Ce-containing steel was more uniform, as shown in Fig. 6a, b. According to Fig. 6c, the average grain size decreased by 10.03% from 13.76 to 12.38  $\mu\text{m}$  after adding Ce. Rare earth can play a role in the refinement of grains [23].



**Table 2** The disregistry calculation parameters and results between inclusions and  $\delta$ -Fe/ $\gamma$ -Fe

Substance	Lattice parameter/nm	Orientation	Disregistry results
$\delta$ -Fe	$a = 0.29315$	–	–
$\gamma$ -Fe	$a = 0.3681$	–	–
CaS	$a = 0.5622$	(111) CaS // (111) $\delta$ -Fe	4.11%
		(111) CaS // (111) $\gamma$ -Fe	52.73%
$MgAl_2O_4$	$a = 0.8085$	(111) $MgAl_2O_4$ // (111) $\delta$ -Fe	37.90%
		(111) $MgAl_2O_4$ // (111) $\gamma$ -Fe	119.64%
$CeAlO_3$	$a = b = 0.3767, c = 0.3797$	(100) $CeAlO_3$ // (100) $\delta$ -Fe	9.14%
		(100) $CeAlO_3$ // (100) $\gamma$ -Fe	2.34%
$Ce_2O_2S$	$a = b = 0.401, c = 0.683$	(0001) $Ce_2O_2S$ // (111) $\delta$ -Fe	3.27%
		(0001) $Ce_2O_2S$ // (100) $\gamma$ -Fe	10.50%



**Fig. 6** IPF color maps and average grain size of the experimental steels: **a** IPF color map of the S1 steel (0 Ce); **b** IPF color map of the S2 steel (0.002% Ce); **c** Average grain size of the experimental steels with different Ce contents

On the basis of the above results, the mechanism of the influence of Ce on the solidification nucleation and microstructure was defined. Without the addition of Ce, the inclusions in the S1 steel were CaS and  $MgAl_2O_4$ , which were not effective in inducing the solidification nucleation. The velocity of solidification phase transformation was slow, and the time for grain growth was sufficient, resulting in the large grains in the solidification microstructure. After Ce treatment, the inclusions in the S2 steel were modified to  $CeAlO_3$  and  $Ce_2O_2S$ , and their disregistry with  $\delta$ -Fe or  $\gamma$ -Fe were all less than 12%. At the initial stage of solidification, the large number of fine rare earth inclusions increased the amount of  $\delta$ -Fe, providing more effective nucleation sites for the formation of  $\gamma$ -Fe in the subsequent peritectic reaction and facilitating the reaction [24]. Meanwhile, rare earth inclusions could also induce the heterogeneous nucleation of  $\gamma$ -Fe at the end of solidification. Consequently, the nucleation site density increased dramatically during solidification. In addition, the increase of phase transformation velocity shortened the solidification time. The nucleated grains did not have time to grow, leading to the refinement of the grains during solidification.

## Conclusions

The effect of cerium on the nucleation and microstructure of high-strength low-alloy steel during solidification were investigated by experimental observations and theoretical calculations. The main results are summarized below:

- (1) The solidification path of the experimental steel was  $L \rightarrow L + \delta \rightarrow L + \delta + \gamma \rightarrow L + \gamma \rightarrow \gamma$ . After 8 and 16 s, the density of nucleation site in the Ce-containing steel was 115.74 and 222.90  $mm^{-2}$ , respectively, which was 47.16 and 115.74  $mm^{-2}$  higher than that of the Ce-free steel. After cerium treatment, the temperature range and time of solidification decreased from 48.1 °C and 52.02 s to 30.5 °C and 29.58 s, respectively.
- (2) According to the JMAK theory, the Avrami exponent  $n$  changed from 2.77 to 2.6 after adding Ce, and the nucleation mechanism was the site saturation nucleation. The addition of Ce increased the solidification rate constant  $k$  from  $7.59 \times 10^{-5}$  to  $5.68 \times 10^{-4}$ , promoting the transformation from liquid to solid phase.
- (3) The typical inclusions in the Ce-free steel were CaS inclusions and  $CaS+MgAl_2O_4$  complex inclusions. In the Ce-containing steel, the typical inclusions were  $CeAlO_3+CaS$  and  $Ce_2O_2S+CaS$  complex inclusions. The average size of inclusions decreased from 2.83 to 1.56  $\mu m$ , and the number density increased from 46.21 to 64.85  $mm^{-2}$  with the addition of Ce.
- (4) Based on the Bramfitt disregistry theory, the disregistry results between rare earth inclusions and  $\delta$ -Fe/ $\gamma$ -Fe were all less than 12%, contributing to the formation of  $\delta$ -Fe and  $\gamma$ -Fe. Upon the addition of rare earth, the large number of fine rare earth inclusions generated could effectively induce the heterogeneous

nucleation of  $\delta$ -Fe and  $\gamma$ -Fe during solidification. Therefore, the microstructure was refined due to the increased number of nucleation and the shortened time of solidification. The average grain size decreased from 13.76 to 12.38  $\mu\text{m}$  with the addition of 0.002% Ce.

**Acknowledgements** The authors are grateful for the financial support of the National Natural Science Foundation of China (No. 52074026).

**Disclosure Statement** No potential conflict of interest was reported by the authors.

**Funding** This work was supported by the National Natural Science Foundation of China (grant number 52074026).

## References

1. Alipooramirabad H, Ghomashchi R, Paradowska A, Reid M (2016) Residual stress-microstructure-mechanical property interrelationships in multipass HSLA steel welds. *J Mater Process Tech* 231:456–467. <https://doi.org/10.1016/j.jmatprotec.2016.01.020>
2. Nathan SR, Balasubramanian V, Malarvizhi S, Rao AG (2016) Effect of tool shoulder diameter on stir zone characteristics of friction stir welded HSLA steel joints. *Trans Indian Inst Metals* 69:1861–1869. <https://doi.org/10.1007/s12666-016-0846-3>
3. Ji YP, Zhang MX, Ren HP (2018) Roles of lanthanum and cerium in grain refinement of steels during solidification. *Metals* 8(11):884. <https://doi.org/10.3390/met8110884>
4. Zhang SH, Yu YC, Wang SB, Li H (2017) Effects of cerium addition on solidification structure and mechanical properties of 434 ferritic stainless steel. *J Rare Earth* 35(5):518–524. [https://doi.org/10.1016/S1002-0721\(17\)60942-6](https://doi.org/10.1016/S1002-0721(17)60942-6)
5. Bartlett LN, Avila BR (2016) Grain refinement in lightweight advanced high-strength steel castings. *Int J Metalcast* 10:401–420. <https://doi.org/10.1007/s40962-016-0048-0>
6. Qu TP, Wang DY, Wang HH, Hou D, Tian J, Hu SY, Su LJ (2021) Interface characteristics between TiN and matrix and their effect on solidification structure. *J Iron Steel Res Int* 28:1149–1158. <https://doi.org/10.1007/s42243-020-00546-2>
7. Wu ZH, Zheng W, Li GQ, Matsuura H, Tsukihashi F (2015) Effect of inclusions' behavior on the microstructure in Al-Ti deoxidized and magnesium-treated steel with different aluminum contents. *Metall Mater Trans B* 46:1226–1241. <https://doi.org/10.1007/s11663-015-0311-4>
8. Shi MH, Kannan R, Zhang J, Yuan XG, Li LJ (2019) Effect of Zr microalloying on austenite grain size of low-carbon steels. *Metall Mater Trans B* 50:2574–2585. <https://doi.org/10.1007/s11663-019-01701-1>
9. Guan QF, Jiang QC, Fang JR, Jiang H (2003) Microstructures and thermal fatigue behavior of Cr-Ni-Mo hot work die steel modified by rare earth. *ISIJ Int* 43(5):784–789. <https://doi.org/10.2355/isijinternational.43.784>
10. Zhao QC, Luo H, Pan ZM, Wang XF, Cheng HX (2023) Study on mechanical properties of rare earth elements modified high carbon chromium bearing steel. *Mater Today Commun* 34:105329. <https://doi.org/10.1016/j.mtcomm.2023.105329>
11. Qiao XY, Han X, He ZJ, Zhuang Z, Yang X, Mao FX (2022) Effect of cerium addition on microstructure and mechanical properties of as-cast high grade knives steel. *J Iron Steel Res Int* 29(12):1986–1994. <https://doi.org/10.1007/s42243-022-00798-0>
12. Zhang JS, Li GQ, Wang HH, Wan XL, Hu MF, Cao YL (2022) Effect of cerium on microstructure and microsegregation behavior of novel cryogenic high-Mn austenitic steel weld metal. *Mater Charact* 194:112427. <https://doi.org/10.1016/j.matchar.2022.112427>

13. Griesser S, Reid M, Bernhard C, Dippenaar R (2014) Diffusional constrained crystal nucleation during peritectic phase transitions. *Acta Mater* 67:335–341. <https://doi.org/10.1016/j.actamat.2013.12.018>
14. Chen HB, Long MJ, Cao JS, Chen DF, Liu T, Dong ZH (2017) Phase transition of peritectic steel Q345 and its effect on the equilibrium partition coefficients of solutes. *Metals* 7(8):288. <https://doi.org/10.3390/met7080288>
15. Liu T, Long MJ, Chen DF, Huang YW, Yang J, Duan HM, Gui LT, Xu P (2020) Investigation of the peritectic phase transition in a commercial peritectic steel under different cooling rates using in situ observation. *Metall Mater Trans B* 51:338–352. <https://doi.org/10.1007/s11663-019-01758-y>
16. Tuttle R (2012) Effect of rare earth additions on grain refinement of plain carbon steels. *Int J Metalcast* 6:51–65. <https://doi.org/10.1007/BF03355527>
17. Christian JW (1965) *The theory of transformations in metals and alloys*. Pergamon Press, Oxford
18. Wang H, Bao YP, Zhao M, Wang M, Yuan XM, Gao S (2019) Effect of Ce on the cleanliness, microstructure and mechanical properties of high strength low alloy steel Q690E in industrial production process. *Int J Min Met Mater* 26:1372–1384. <https://doi.org/10.1007/s12613-019-1871-0>
19. Zhuo C, Liu R, Zhao ZR, Zhang YL, Hao XS, Wu HJ, Sun YH (2022) Effect of rare earth cerium content on manganese sulfide in U75V heavy rail steel. *Metals* 12(6):1012. <https://doi.org/10.3390/met12061012>
20. Bramfitt BL (1970) The effect of carbide and nitride additions on the heterogeneous nucleation behavior of liquid iron. *Metall Trans* 1:1987–1995. <https://doi.org/10.1007/BF02642799>
21. Gao JZ, Fu PX, Liu HW, Li DZ (2015) Effects of rare earth on the microstructure and impact toughness of H13 steel. *Metals* 5(1):383–394. <https://doi.org/10.3390/met5010383>
22. Yang J, Hao FF, Li D, Zhou YF, Ren XJ, Yang YL, Yang QX (2012) Effect of RE oxide on growth dynamics of primary austenite grain in hardfacing layer of medium-high carbon steel. *J Rare Earth* 30(8):814–819. [https://doi.org/10.1016/S1002-0721\(12\)60136-7](https://doi.org/10.1016/S1002-0721(12)60136-7)
23. Xin WB, Zhang J, Luo GP, Wang RF, Meng QY, Song B (2018) Improvement of hot ductility of C-Mn Steel containing arsenic by rare earth Ce. *Metall Res Technol* 115(4):419. <https://doi.org/10.1051/metal/2018030>
24. Torkamani H, Raygan S, Garcia MC, Rassizadehghani J, Palizdar Y, San-Martin D (2018) Contributions of rare earth element (La, Ce) addition to the impact toughness of low carbon cast niobium microalloyed steels. *Met Mater Int* 24:773–788. <https://doi.org/10.1007/s12540-018-0084-9>